Quarterly Journal of the Royal Meteorological Society Q. J. R. Meteorol. Soc. 140: 2147–2157, October 2014 A DOI:10.1002/qj.2285

RMetS
Royal Meteorological Society

Non-normal growth of Kelvin–Helmholtz eddies in a sea breeze

Yizhak Feliks,[a]* Eli Tziperman[b] and Brian Farrell[b]

[a]*Department of Mathematics, Israel Institute for Biological Research, Ness-Ziona, Israel*
[b]*Department of Earth and Planetary Sciences and School of Engineering and Applied Sciences, Harvard University, Cambridge, MA, USA*

*Correspondence to: Y. Feliks, Department of Mathematics, Israel Institute for Biological Research, PO Box 19, Ness-Ziona, Israel 70450. E-mail: feliks@iibr.gov.il

The generalized stability of a sea-breeze front is analyzed using a two-dimensional model. The objective is to understand the mechanisms leading to the shedding of eddies behind the sea-breeze front, as seen in observations, laboratory experiments and numerical models. Regions with $Ri < 1/4$ are not always associated with instability in this spatially inhomogeneous flow and significant transient growth is found in the absence of normal-mode instability, for both $Ri \leq 1/4$ and $Ri > 1/4$. The energy source for optimal growth is the vertical shear of the mean horizontal wind, the vertical shear in the upper part of the front and the horizontal shear in the lower part. The growth begins with vertical advection by the perturbation velocity of the mean flow momentum located in the upper part of the front. Perturbations eventually propagate away from the localized shear area and a feedback mechanism is needed for this growth to be sustained. This feedback occurs through temperature anomalies in the upper part of the front inducing pressure-gradient anomalies in the lower part. These gradients lead to a growing vertical wind component and this vertical wind component then enters the upper part of the front, which reinforces the extraction of energy, thereby closing the feedback loop and leading to both normal-mode instability and, in the stable regime, large non-normal growth. We find that both the instability and the non-normal growth are vulnerable to parameter changes that weaken this feedback loop.

Key Words: Kelvin–Helmholtz eddies; non-normal growth; sea breeze

Received 31 March 2013; Revised 14 October 2013; Accepted 18 October 2013; Published online in Wiley Online Library 12 February 2014

1. Introduction

Sea-breeze dynamics have been extensively studied using observations as well as analytical and numerical models (e.g. Atkinson, 1981). The sea-breeze frontal region is strongly turbulent and is characterized by extensive mixing between cool and humid sea air and dry and warm land air. This frontal region is an example of a density current (also known as a gravity current), other examples of which include cold gust fronts in thunderstorm outflows and ocean overflows. Density currents have been extensively studied in the laboratory (Simpson, 1969, 1972; Simpson and Linden, 1989; Britter and Simpson, 1978, 1981; Britter and Linden, 1980; Linden and Simpson, 1986). Several eddies are typically seen behind the leading edge of density currents, in both observations (Lapworth, 2000; Plant and Keith, 2007) and numerical simulations (Sha *et al.*, 1991; Buckley and Kurzeja, 1997a, 1997b) These eddies have usually been identified with billows due to Kelvin–Helmholtz (K–H) instability.

Xue *et al.* (1997) showed in numerical simulations that, in the presence of strong shear at the density-current interface, K–H like billows are shedding periodically at the back edge of the elevated head of the advancing density current. As these billows move backward, they lead to an entrainment of lighter air from above into the denser air below (see figure 6(a) of Xue *et al.*, 1997), producing a mixed transition layer that is roughly half the depth of the head of the advancing gravity current (figure 6(b) of Xue *et al.*, 1997). Such billows are characteristic of numerically simulated density currents in high-resolution models (Droegemeier and Wilhelmson, 1987; Xu *et al.*, 1996) as well as in laboratory experiments (Benjamin, 1968; Britter and Simpson, 1978).

The horizontal wavelength of the fastest growing perturbation in a shear layer of thickness h has been shown to range from $4.4h$ (Drazin, 1958) to $7.5h$ (Miles and Howard, 1964), which has been argued to be consistent with K–H instability (Droegemeier and Wilhelmson, 1987; Mueller and Carbone, 1987; Sha *et al.*, 1991). Similar length-scales were also observed in thunderstorms (Droegemeier and Wilhelmson, 1987) and in laboratory gravity-current experiments (Xue *et al.*, 1997; Maxworthy *et al.*, 2002). However, in these studies no explicit stability analysis was performed and the inference of a K–H instability was based on satisfying the necessary condition for instability, i.e. that the Richardson number,

$$Ri = \frac{g}{\theta_{\mathrm{m}}} \frac{\partial \bar{\theta}}{\partial z} \Big/ \left(\frac{\partial \bar{u}}{\partial z}^2 + \frac{\partial \bar{v}}{\partial z}^2 \right), \tag{1}$$

is less than the critical value, $Ri < 1/4$. On the other hand, both observations (Lapworth, 2000) and simulations (Sha *et al.*, 1991; Xue *et al.*, 1997) reveal that disturbances resembling Kelvin–Helmholtz eddies arise and grow in regions where $1/4 < Ri < 1$, larger than the critical value associated with the necessary condition for K–H instability.

Farrell and Ioannou (1993) examined the generalized stability and transient non-normal growth as a function of Ri for background states with constant shear and stratification. They found substantial growth of perturbations in shear flows even for $Ri = \mathcal{O}(1)$ and that for such transient growth no special significance is attached to $Ri = 0.25$.

The purpose of this article is to examine normal and non-normal growth of eddies behind the leading edge of a sea-breeze front. We show that these eddies develop in stable as well as in unstable flows and that non-normal growth can explain observations of turbulent flow with $Ri > 0.25$. We also show that flows are often stable even when $Ri < 0.25$. Finally, we discuss the instability mechanism of a sea-breeze front and show that it must be different from the classical K–H instability in some major aspects.

We use a nonlinear model to find the basic state of the sea-breeze front, but our stability analysis is linear. While we show that many observed features can be explained within this linear framework, it is known that nonlinearities can be important to many aspects of the sea-breeze circulation. Nonlinearity influences the evolution of frontal structure and its inland propagation, which were studied numerically by Estoque (1961), Pearson (1973), Physick (1976) and Neumann and Mahrer (1971) and analytically by Feliks (1988, 2000).

In the following sections we describe the model equations (section 2), analyze the growth mechanism in the unstable case (section 3) then discuss non-normal growth in the stable regime (section 4) and conclude in section 5.

2. Model equations

We study the generalized stability of a propagating front in the (x, z) plane, where x is the cross-coast direction and z is the vertical. The front and perturbations are assumed homogeneous in the along-coast (y) direction. This simplification is consistent with the typical observed cross-coastal length-scale being about 50 km, while the scale in the along-coast direction is often larger by an order of magnitude. We first use a nonlinear time-dependent model to calculate the base state of the sea breeze and then proceed to linearize and simplify these equations for the stability analysis. The nonlinear Boussinesq incompressible hydrostatic approximation model equations are

$$\begin{aligned}
\frac{\partial u}{\partial t} + u\frac{\partial u}{\partial x} + w\frac{\partial u}{\partial z} - fv &= -\frac{1}{\rho_\mathrm{m}}\frac{\partial p}{\partial x} + K_\mathrm{h}\frac{\partial^2 u}{\partial x^2} + K_\mathrm{v}\frac{\partial^2 u}{\partial z^2},\\
\frac{\partial v}{\partial t} + u\frac{\partial v}{\partial x} + w\frac{\partial v}{\partial z} + fu &= K_\mathrm{h}\frac{\partial^2 v}{\partial x^2} + K_\mathrm{v}\frac{\partial^2 v}{\partial z^2},\\
\frac{\partial u}{\partial x} + \frac{\partial w}{\partial z} &= 0,\\
\frac{1}{\rho_\mathrm{m}}\frac{\partial p}{\partial z} &= -\frac{g\rho}{\rho_\mathrm{m}},\\
\frac{\theta}{\theta_\mathrm{m}} &= -\frac{\rho}{\rho_\mathrm{m}},\\
\frac{\partial \theta}{\partial t} + u\frac{\partial \theta}{\partial x} + w\frac{\partial \theta}{\partial z} &= K_\mathrm{h}\frac{\partial^2 \theta}{\partial x^2} + K_\mathrm{v}\frac{\partial^2 \theta}{\partial z^2}.
\end{aligned} \tag{2}$$

The pressure is calculated from the hydrostatic equation. The wind components in the (x, y, z) directions are u, v and w. The diffusion coefficients in the horizontal and vertical are $K_\mathrm{h} = 5 \times 10^2\ \mathrm{m^2\,s^{-1}}$ and $K_\mathrm{v} = 1\ \mathrm{m^2\,s^{-1}}$, respectively. We choose constant diffusion coefficients in order to simplify the analysis. There are many formulations of the vertical diffusion coefficient as a function of height z. Since the fit of the results with these formulations to observations is controversial (Jeričević and Večenaj, 2009), we used the simplest constant-coefficient approximation and we study the sensitivity of the mechanism to the value of this coefficient; see the additional discussion in the appendix. The Coriolis parameter is $f = 14.585 \times 10^{-5} \sin(32^\circ)$ and $g = 9.81\ \mathrm{m\,s^{-2}}$ is the acceleration of gravity. Reference values of the potential temperature and density are $\theta_\mathrm{m} = 300\ \mathrm{K}$ and $\rho_\mathrm{m} = 1.3\ \mathrm{kg\,m^{-3}}$, respectively. The lower boundary condition parametrizes a constant-stress surface layer (below our first model level, see appendix) in which the stress is given by a surface drag law with drag coefficient $C_\mathrm{D} = 10^{-3}$ over water and $C_\mathrm{D} = 10^{-2}$ over land, so that

$$\begin{aligned}
K_\mathrm{v}\frac{\partial u}{\partial z}\bigg|_h &= C_\mathrm{D}\sqrt{u_h^2 + v_h^2}\,u_h,\\
K_\mathrm{v}\frac{\partial v}{\partial z}\bigg|_h &= C_\mathrm{D}\sqrt{u_h^2 + v_h^2}\,v_h,
\end{aligned} \tag{3}$$

where u_h and v_h are the components of the surface velocity at the top of the first grid box, $z = h$. We specify $w = 0$ at $z = 0$. The upper boundary is taken to be at a height of 5440 m and is assumed to be a rigid lid (where $w = 0$ as well), with u and v set there to specified values representing a uniform geostrophic wind u_g and v_g. The potential temperature at the upper boundary is held constant at $\theta = 318.4\ \mathrm{K}$ and p is determined there from the prescribed wind using geostrophic balance. The sea-surface temperature is assumed constant, while the ground temperature is prescribed to vary periodically to simulate a diurnal cycle:

$$\theta(x,t) = \begin{cases} 300\ \mathrm{K} + \theta_0 \sin(\omega t) & x > 0\ \text{(land)},\\ 300\ \mathrm{K} & x < 0\ \text{(sea)}, \end{cases} \tag{4}$$

where $\omega = 2\pi/24h$ and $t = 0$ is the time at which the prescribed land and sea temperatures in Eq. (4) are equal (approximately the time of sunrise; see the discussion in the appendix). The model extends in the x direction for 50 km over the sea and 50 km over land and $x = 0$ is the coast location. At the seaward and landward side boundaries, the normal derivatives of u, v and θ are set to zero. Convective adjustment is applied during the model integration when the vertical gradient of the potential temperature falls below $10^{-2}\ \mathrm{K\,km^{-1}}$ and therefore maintains the atmosphere in a weakly stable state. Numerical details are summarized in the appendix.

In the first experiment considered below, the geostrophic velocities prescribed on the upper boundary are $u_\mathrm{g} = -1.9\ \mathrm{m\,s^{-1}}$, $v_\mathrm{g} = 0$ and the amplitude of the diurnal cycle in land temperature is set to $\theta_0 = 4.5\ \mathrm{K}$. We integrated the model for 200 days until it approached a nearly periodic diurnal solution. Some very weak, seemingly chaotic, variability due to model nonlinearity remains, possibly due to an interaction with inertial oscillations as shown by Feliks (2004). We averaged the state at $t = 8\ \mathrm{h}$ over the last 40 days to eliminate this variability and used this average as our base state. Figure 1 shows the circulation, averaged over the last 40 days, at times during the day when the front is most developed, showing that the circulations over sea and land are reasonably realistic and similar to those reported in previous studies (e.g. Estoque, 1961; Pearson, 1973; Physick, 1976; Neumann and Mahrer, 1971; Sha *et al.*, 1991). The front propagates inland at an almost constant speed of $c = 1\ \mathrm{km\,h^{-1}}$ and its shape is not significantly changed while propagating. To simplify the study of the generalized stability of the front, we therefore assume that (i) the front keeps its spatial structure while propagating and (ii) the front propagates at a constant speed and we examine the evolution of perturbations to the propagating front in a coordinate frame moving at that same speed.

We choose the mean state for our experiment 1 below to be the nonlinear solution at $t = 8\ \mathrm{h}$ (i.e. 8 h after the ocean and land temperatures are equal, or about 8 h past sunrise). Now let

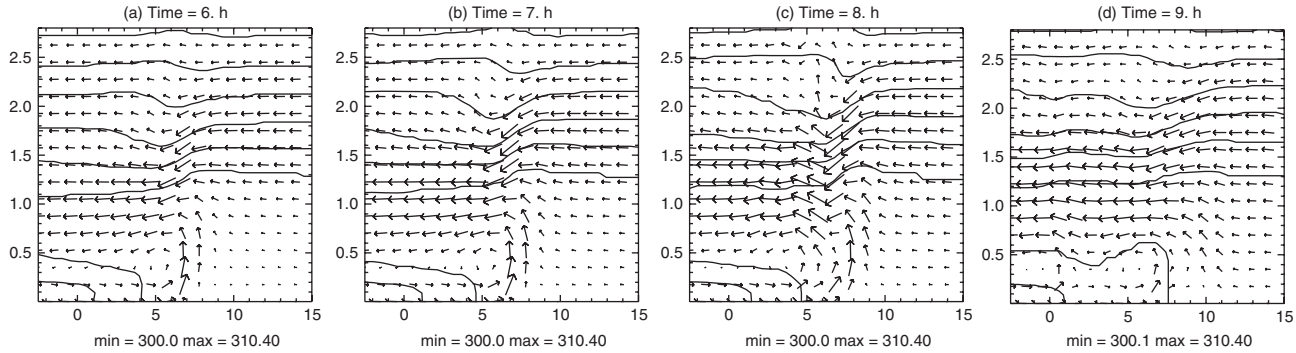

Figure 1. The mean sea-breeze circulation for experiment 1 (analysis of normal-mode instability and non-normal growth). The times during the day at which the front is most prominent are shown. Both axes (x, z) are in km, contours are of potential temperature, the contour interval is 1 K and arrows represent the (u, w) wind velocities. Note that the computational domain extends from −50 to 50 km and only part of it is plotted here, to allow focusing on the front structure.

$\theta = \bar{\theta} + \theta'$, where $\bar{\theta}$ is the mean state potential temperature and θ' is the perturbation potential temperature; similarly, introduce small perturbations to the other fields. When written in the moving coordinate frame, where x is replaced by $x - ct$ and $\bar{u}$ by $\bar{u} - c$, under the above two simplified assumptions the horizontal advection terms take the form $(\bar{u} + c)\partial A'/\partial x$, where A' stands for u', v' or θ'. With the model equations linearized about $(\bar{u}, \bar{v}, \bar{\theta})$, the perturbation equations are

$$\begin{aligned}
&\frac{\partial u'}{\partial t} + \bar{u}\frac{\partial u'}{\partial x} + u'\frac{\partial \bar{u}}{\partial x} + \bar{w}\frac{\partial u'}{\partial z} + w'\frac{\partial \bar{u}}{\partial z} - fv' \\
&\qquad = -\frac{1}{\rho_m}\frac{\partial p'}{\partial x} + K_h\frac{\partial^2 u'}{\partial x^2} + K_v\frac{\partial^2 u'}{\partial z^2}, \\
&\frac{\partial v'}{\partial t} + \bar{u}\frac{\partial v'}{\partial x} + u'\frac{\partial \bar{v}}{\partial x} + \bar{w}\frac{\partial v'}{\partial z} + w'\frac{\partial \bar{v}}{\partial z} + fu' \\
&\qquad = K_h\frac{\partial^2 v'}{\partial x^2} + K_v\frac{\partial^2 v'}{\partial z^2}, \\
&\frac{\partial u'}{\partial x} + \frac{\partial w'}{\partial z} = 0, \\
&\frac{1}{\rho_m}\frac{\partial p'}{\partial z} = -\frac{g\rho'}{\rho_m}, \\
&\frac{\theta'}{\theta_m} = -\frac{\rho'}{\rho_m}, \\
&\frac{\partial \theta'}{\partial t} + \bar{u}\frac{\partial \theta'}{\partial x} + u'\frac{\partial \bar{\theta}}{\partial x} + \bar{w}\frac{\partial \theta'}{\partial z} + w'\frac{\partial \bar{\theta}}{\partial z} \\
&\qquad = K_h\frac{\partial^2 \theta'}{\partial x^2} + K_v\frac{\partial^2 \theta'}{\partial z^2}.
\end{aligned} \tag{5}$$

We linearize the lower boundary condition (3) to find

$$\begin{aligned}
K_v\left.\frac{\partial u'}{\partial z}\right|_h &= C_D(2\bar{u}_h^2 + \bar{v}_h^2)/\sqrt{\bar{u}_h^2 + \bar{v}_h^2}\,u'_h, \\
K_v\left.\frac{\partial v'}{\partial z}\right|_h &= C_D(\bar{u}_h^2 + 2\bar{v}_h^2)/\sqrt{\bar{u}_h^2 + \bar{v}_h^2}\,v'_h.
\end{aligned} \tag{6}$$

The perturbation vertical velocity, w', and potential temperature, θ', vanish at the upper and lower boundaries. At the side boundaries the normal derivatives of u', v' and θ' are set to zero, as in the fully nonlinear model (see the appendix for more details).

We denote the domain average, the integral over the volume divided by the (x, z) domain area, by $\langle\rangle$; [] denotes an integral with respect to z divided by the domain height; and $\{\}_{x_e}^{x_w}$ denotes the difference of the enclosed term between the horizontal boundaries (i.e. the net flux into the domain through the vertical side boundaries) divided by domain length. Further, define $\alpha = g\left(\theta_m \partial\bar{\theta}/\partial z\right)^{-1}$ and the kinetic, potential and total domain-averaged energies (J m^{-2}) are

$$\begin{aligned}
\langle E_k\rangle &= \frac{1}{2}\langle u'^2 + vP'^2\rangle, \\
\langle E_p\rangle &= \frac{1}{2}\langle \alpha\theta'^2\rangle, \\
\langle E_T\rangle &= \frac{1}{2}\langle u'^2 + v'^2 + \alpha\theta'^2\rangle.
\end{aligned} \tag{7}$$

The derivations of the kinetic and potential energy equations are given in the appendix. The rate of transfer between kinetic and potential energy is given by

$$\left\langle w'\theta'\frac{g}{\theta_m}\right\rangle \tag{8}$$

and the total energy equation for our set of equations is the sum of kinetic and potential energy equations (A2) and (A3), given by

$$\begin{aligned}
\frac{\partial\langle E_T\rangle}{\partial t} = &-\langle u'^2\frac{\partial \bar{u}}{\partial x}\rangle - \langle u'w'\frac{\partial \bar{u}}{\partial z}\rangle \\
&-\langle v'u'\frac{\partial \bar{v}}{\partial x}\rangle - \langle v'w'\frac{\partial \bar{v}}{\partial z}\rangle - \langle \alpha\theta'u'\frac{\partial \bar{\theta}}{\partial x}\rangle \\
&+\frac{1}{2}\left\langle\left(\theta'^2\bar{u} + K_h\frac{\partial\theta'^2}{\partial x}\right)\frac{\partial\alpha}{\partial x}\right\rangle \\
&+\frac{1}{2}\left\langle\left(\theta'^2\bar{w} + K_v\frac{\partial\theta'^2}{\partial z}\right)\frac{\partial\alpha}{\partial z}\right\rangle \\
&-K_h\left(\left\langle\left(u'_x\right)^2\right\rangle + \left\langle\left(v'_x\right)^2\right\rangle + \left\langle\alpha\left(\theta'_x\right)^2\right\rangle\right) \\
&-K_v\left(\left\langle\left(u'_z\right)^2\right\rangle + \left\langle\left(v'_z\right)^2\right\rangle + \left\langle\alpha\left(\theta'_z\right)^2\right\rangle\right) \\
&+\left\{\left[\frac{1}{\rho_m}u'p' + \bar{u}u'^2 + \bar{u}v'^2 + \bar{u}\alpha\theta'^2\right]\right\}_{x_w}^{x_e}.
\end{aligned} \tag{9}$$

2.1. *Optimal initial conditions and linear stability*

Using finite differencing, the linearized equations for u', v' and θ' (Eq. (3)) may be written in vector form as

$$\mathsf{B}\mathbf{P}_{n+1} = \mathsf{B}\mathbf{P}_n = \mathsf{B}^n\mathbf{P}_0, \tag{10}$$

where $\mathbf{P}$ is the state vector of anomalies on the model's 2D grid:

$$\mathbf{P} = [u'_1, u'_2 \ldots u'_k, v'_1, v'_2 \ldots v'_k, \theta'_1, \theta'_2 \ldots \theta'_k], \tag{11}$$

where k is the total number of grid points and B is the $3k\times3k$ propagator (matrix) of the finite-difference linearized model.

Write the total energy integrated over the domain (Eq. (7)) as

$$\langle E_T\rangle = \mathbf{P}(\tau)^T\mathsf{X}\mathbf{P}(\tau),$$

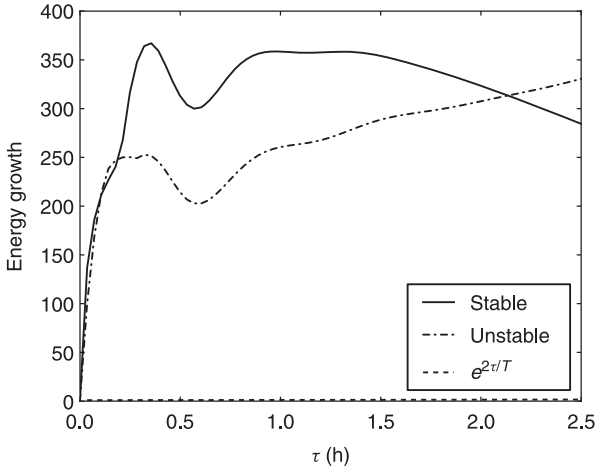

Figure 2. Total energy growth factor as a function of optimization time τ. The results of experiment 2, in which the propagator is stable, and experiment 1, in which the propagator is unstable, are shown. Also shown is the initial total energy of the optimal initial conditions ($E_T(0)$, set to one) times an exponential growth factor $E_T(0)\exp(2\tau/T)$, where T is the growth time-scale obtained from the most unstable eigenvalue of the propagator B of experiment 1. The growth due to normal-mode instability is seen to be much slower than the non-normal growth.

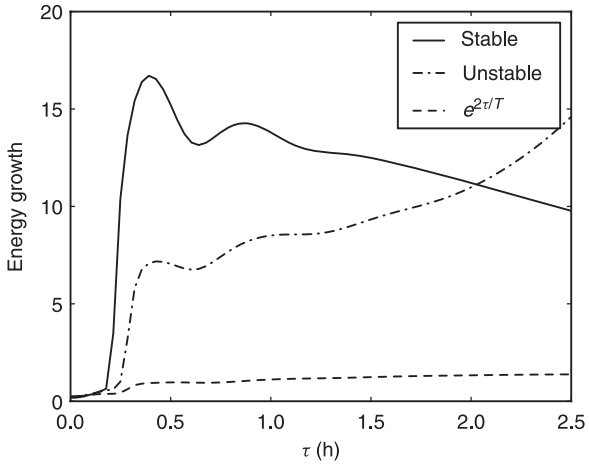

Figure 3. Kinetic energy growth factor; curves are as in Figure 2. The dashed line denotes the initial kinetic energy of the optimal initial conditions (for which $E_T(t=0,\tau)$ is equal to one) times an exponential growth factor $E_k(t=0,\tau)\exp(2\tau/T)$.

where the matrix X is known as the energy-norm kernel. Optimal initial conditions are those that maximize the state vector norm $\mathbf{P}(\tau)^{\mathrm{T}}\mathsf{X}\mathbf{P}(\tau)$ at a time $\tau = n\Delta t$, where $\Delta t = 1$ s is the model time step, subject to a constraint on the initial conditions $\mathbf{P}(0)^{\mathrm{T}}\mathsf{Y}\mathbf{P}(0) = 1$. Y may, in principle, be a different norm kernel constraining the amplitude of the optimal initial condition. The optimal initial conditions in the non-normal growth problem are the solution of the eigenproblem (Farrell, 1988, 1989; Farrell and Ioannou, 1996)

$$\mathsf{Y}^{-1}\mathsf{B}^{n\mathrm{T}}\mathsf{X}\mathsf{B}^{n}\mathbf{e} = \lambda\mathbf{e} \tag{12}$$

with the largest eigenvalue λ. Unstable normal modes are eigenvectors of B itself, whose eigenvalues are larger than one in absolute value. The unstable mode is almost perpendicular to the optimal initial condition $\mathbf{e}$ found in the non-normal growth problem. One can also analyze the propagator using singular-value decomposition (SVD: Farrell and Ioannou, 1996), revealing additional interesting properties of the non-normal dynamics.

3. Analysis of unstable normal-mode growth mechanism and comparison with classical K–H instability

We find that the nonlinear solution at $t = 8$ h may be stable or unstable depending on the value of the specified geostrophic velocity at the top of the domain, u_g. Similarly, the basic state may also allow for non-normal growth, depending on the value of u_g. We wish to explain the mechanism by which this occurs. We consider first the regime for $u_g \le -1\,\mathrm{m\,s^{-1}}$, which is characterized by a sharp front structure that always allows for non-normal growth and may be either stable or unstable for different values of $u_g \le -1$. For this parameter regime, we first explore the normal-mode instability mechanism and show that it is qualitatively different from the classical K–H mechanism. This mechanism is also responsible for non-normal growth in the parameter regime in which the model is modally stable, which is analyzed in the following subsection. We then show that even in the unstable regime the non-normal amplification dominates the growth.

Setting u_g to $-1.9\,\mathrm{m\,s^{-1}}$ (experiment 1 in Table 1), the eigenvalue with largest absolute value of the propagator B (Eq. (10)) is

$$\lambda = |\lambda|e^{\mathrm{i}\phi} = \lambda_r + \mathrm{i}\lambda_i = 1.000028 + 0.0000985\,\mathrm{i}.$$

This complex eigenvalue implies an oscillatory behaviour and translates into an exponential growth time of about $\Delta t/\ln|\lambda| =$ 9.9 h and an oscillation period $2\pi\Delta t/\phi = 17$ h ($\Delta t = 1$ s is the model time step). If normal-mode instability is the main contributor to the growth, we expect the energy growth factor to be e^2 after 9.9 h. The norm used in the experiments of this section is the total energy norm (E_T) based on Eq. (7). Energy growth factors for the total, kinetic and potential energies are defined as

$$\text{growth factor}_{\{\mathrm{T,k,p}\}} = \langle E_{\{\mathrm{T,k,p}\}}(t)\rangle/\langle E_T(0)\rangle,$$

where the initial perturbation is the one leading to optimal growth at $t = \tau$ and τ is referred to as the optimization time. Figures 2 and 3 show that the growth factor is larger than the normal-mode growth predicts by two orders of magnitude even after two and half hours, implying that energy growth is due to non-normal dynamics even in the unstable regime. At later times normal growth eventually dominates, of course, if the mean state is unstable (Farrell and Ioannou, 1996). Still, the integration starting from the optimal initial conditions maintains its lead at later times over the one starting with the most unstable eigenvector structure, although both have the same unit initial amplitude as measured by the energy norm, $\mathbf{P}(0)^{\mathrm{T}}\mathsf{X}\mathbf{P}(0) = 1$.

Figures 4 and 5 show the optimal initial perturbation for $\tau = 1$ h and its evolution at selected times. The perturbation circulation is composed of two eddy-like features. One is completely contained within the lower 1500 m or so on the landward side. The second, clockwise eddy, is found above the first eddy and a third eddy splits from the seaward part of the second eddy (Figure 4(b)) and is advected seaward (Figure 4(b)–(d)). This structure is reminiscent of observations of shedding seaward-propagating K–H billows behind fronts (Lapworth, 2000; Plant and Keith, 2007). At later times, the new formed eddies reverse direction and continue to grow via the same mechanism. Figure 6 shows the structure of the most unstable normal mode. The structure of the eddies in Figures 4 and 5 is very similar to a linear combination of the real and imaginary parts of this most unstable mode and they are the dominant feature in the model evolution (Figure 4) for $t > 0.5$ h.

In the classical K–H normal-mode instability, a perturbation of harmonic form in x is assumed to exist in a shear flow with stable or neutral stratification in which the shear is unbounded in the shear-parallel (x) direction. The mode energy then grows via the shear production term $-\langle u'w'\partial\bar{u}/\partial z\rangle$ (Eq. (9)) but the structure of the mode is constrained by the stratification, such that for $Ri > 0.25$ the mode is necessarily stable while for $Ri < 0.25$ the mode may be unstable. Interestingly, the unstable and growing eddies in our model are partially or completely contained in regions with $Ri > 0.25$ (cf. the unstable mode in Figure 6). Consistently, detailed analysis shows that the extraction of kinetic

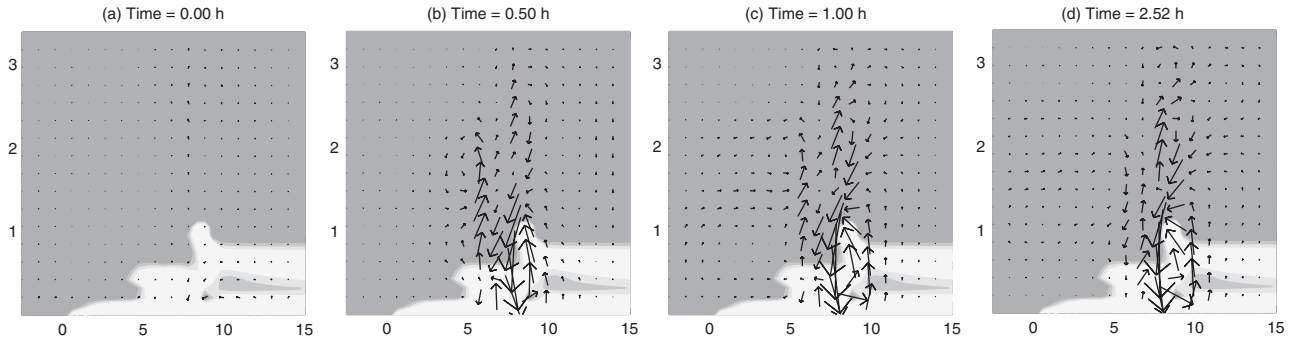

Figure 4. The evolution of the optimal perturbation of experiment 1 at selected times. Grey areas indicate $Ri > 0.25$, arrows denote u', w'. The absolute value of the perturbation is not meaningful, as it reflects the linearized dynamics.

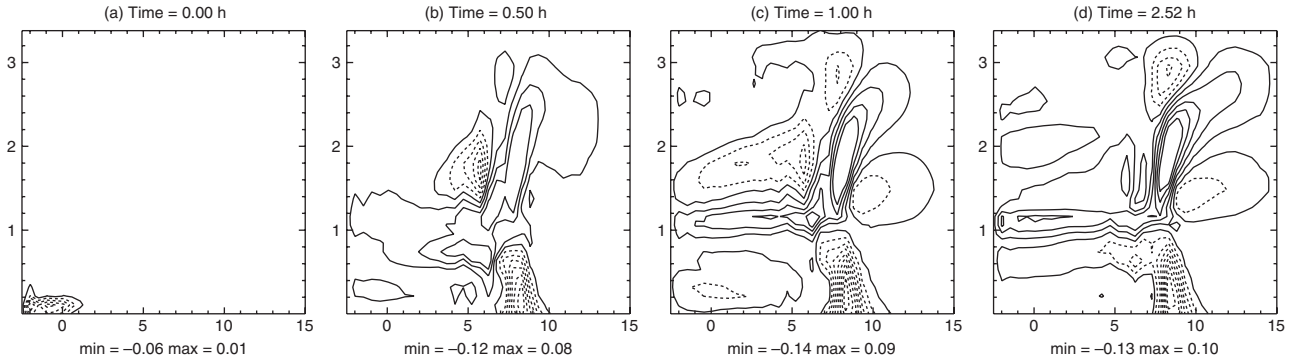

Figure 5. Contours showing the evolution of potential temperature for the optimal perturbation of experiment 1 at selected times. Solid contours are positive and dashed contours are negative. The contour interval is 0.0075 in (a) and 0.015 in (b)–(d).

and potential energy from the mean occurs in regions with $Ri > 0.25$.

3.1. *The instability mechanism*

Consider now the instability mechanism for the unstable growth in our case, using the regions in the (x, z) plane outlined by the white rectangles in Figure 7. Region A, where we find the perturbation growth to be substantial (not only where $Ri < 0.25$), is finite in spatial extent and the perturbations eventually exit it. In order to create sustained growth and therefore an instability, a mechanism that feeds these perturbations back to the locally unstable part of region A is required. We first describe this mechanism qualitatively and then demonstrate it in more detail using the model results.

This feedback loop is closed and augmented by the growth of perturbations in region B, which is contained within the boundary layer. The amplification of u' in the seaward part of region B is mainly due to the pressure gradient, $\partial p'/\partial x$. This boundary-layer pressure gradient, in turn, is determined by θ' in A via the hydrostatic equation. In the landward part of region B, amplification of u' is mainly due to horizontal shear of the mean flow term $-u'\partial\bar{u}/\partial x$. The amplified u' in B results in an increase in the horizontal derivative of u' near the landward side of B, which then leads to a growing w' at the top of B and also in the lower part of A. The growing w' in A causes further growth of u' and θ' there via the energetic term discussed above associated with the vertical shear. Thus, anomalies in region A enhance perturbations in B and vice versa and this closes the feedback loop that enables indefinite normal-mode instability to occur.

To summarize the instability feedback loop: perturbations in region A grow by extracting energy from the mean vertical shear and stratification; region A affects region B by determining its pressure gradient via θ' in A; region B affects A by inducing a growing w' that feeds back into A, completing the feedback loop.

The deciphering of the above mechanism is complicated because the terms leading to growth in regions A and B are not necessarily the locally and instantaneously dominant terms in the momentum and energy equations. We note that the dynamics cannot be diagnosed unambiguously to identify local growth mechanisms by examining the terms in the energy equation, whether expressed in terms of perturbation fluxes or in terms of flux divergence. This is because energy can transfer from a source region to another region by a variety of mechanisms including pressure forces and wave momentum fluxes. In order

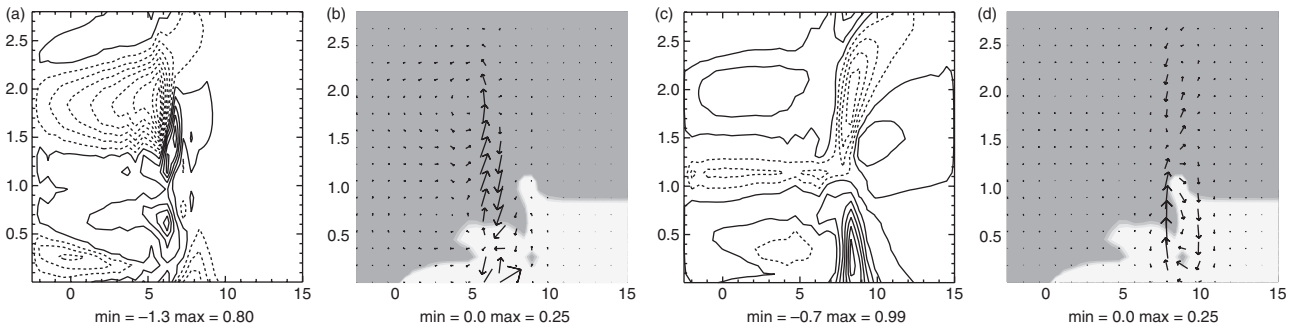

Figure 6. The structure of the unstable mode. Panels (a) and (b) show the real part, while (c) and (d) show the imaginary part. Grey areas in (b) and (d) indicate $Ri > 0.25$, arrows denote u', w'. Contours of potential temperature are shown in (a) and (c); the contour interval is 0.15.

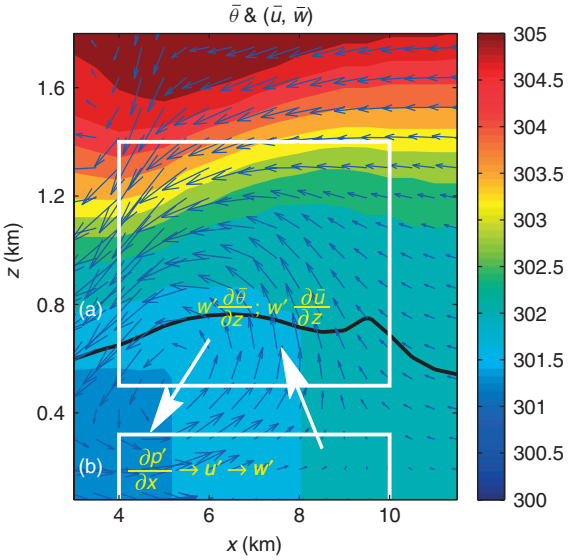

Figure 7. A schematic of the growth mechanism involving interaction between a K–H like growth mechanism in the upper part (rectangle A) and the feedback via the lower part (B). Above the thick black contour line $R_i > 1/4$ and below it $R_i < 1/4$. While this schematic provides the essential part of the feedback loop leading to non-normal growth and to normal-mode instability, some additional terms are found to contribute significantly to the instability mechanism. These are $\partial p'/\partial x$ in the upper part (A) and $w'\partial\bar{u}/\partial z$ and $u'\partial\bar{u}/\partial x$ in the lower part of the sea-breeze front (B).

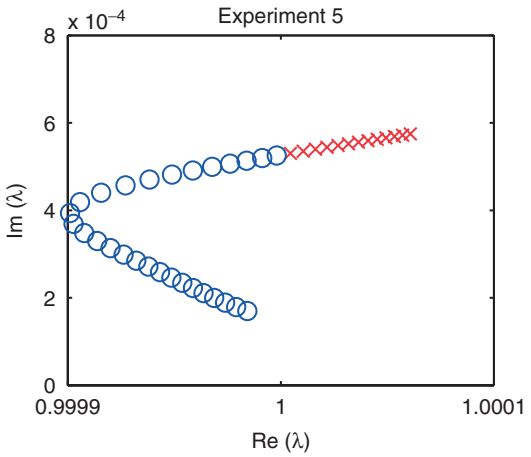

Figure 8. Example of determining the importance of specific terms in the momentum equation to the growth mechanism. In this example the term $\partial p'/\partial x$ is multiplied by a factor γ, which is varied between 1 and 0 in steps of 0.025. Circles (○) indicate a stable model regime and crosses (×) mark an unstable one.

to get around this difficulty in interpretation and demonstrate the above picture of the instability feedback loop, we performed a set of experiments as described in Table 1, in which we turn off different terms in the linearized equations and observe the stability consequences. We multiply a given term by a weight γ and gradually vary this weight between 1 and 0 and follow the change of the largest unstable eigenvalue of the propagator B (Eq. (10)) as the term being examined is gradually decreased. Table 1, experiments 3–8, shows the different terms analyzed this way and Figure 8 shows the results of this analysis for one of the experiments. The most unstable eigenvalue (λ) of the propagator B for $\gamma = 1$ is calculated and is then tracked and plotted as γ gradually goes to zero. This eigenvalue represents a specific physical mode (the structure of which is given by the corresponding eigenvector) and therefore a specific growth mechanism. If this specific mode is stabilized as γ is reduced (as is indeed the case in this example), this indicates that term multiplied by γ is indeed critical to the growth mechanism. Note that, as the once-largest eigenvalue changes with γ and is tracked in the analysis, it does not necessarily remain the largest eigenvalue any more. Using this analysis, we identify which terms are essential to the instability. These essential terms are indicated in Figure 7 and their contribution to the growth is further discussed in section 4.

The instability analyzed here is distinct from the classical K–H instability in several ways. Firstly, crucial energy for the growing perturbations comes from the terms $u'u'\partial\bar{u}/\partial x$ and $\theta'u'\partial\bar{\theta}/\partial x$ in Eq. (9), which represent the extraction of kinetic and potential energy from the horizontal gradients within the front (see the analysis in section 4) rather than only from the vertical gradient as in the K–H case. Secondly and more importantly, our domain is finite and perturbations are advected out of the unstable region and therefore would not grow exponentially in time without the feedback loop discussed above. This feedback loop may be said to allow 'absolute instability', i.e. the perturbations grow in time at every fixed point in the domain, as opposed to 'convective instability', where even though the overall norm of the perturbation grows in time, perturbations decay locally at every fixed point in the unbounded domain. In other words, the growing perturbation is transported, or convected, towards infinity (Briggs, 1964; Merkine, 1977; Farrell, 1982).

Table 1. List of experiments and corresponding model parameters. A and B denote the rectangles shown in Figure 7.

#	u_g (m s^{-1})	Description	Results
1	−1.9		Unstable
1a–f	[−3.5, 1]	sensitivity to u_g	Stable or unstable
2	−2.		Stable non-normal growth
3	−1.9	$u'\frac{\partial\bar{u}}{\partial x} = 0$ in B	Oscillatory mode stabilized, stable solution
4	−1.9	$w'\frac{\partial\bar{u}}{\partial z} = 0$ in B	Oscillatory mode stabilized, stable solution
5	−1.9	$\frac{\partial p'}{\partial x} = 0$ in B	Oscillatory mode stabilize stable solution
6	−1.9	$w'\frac{\partial\bar{u}}{\partial z} = 0$ in A	Oscillatory mode stabilized, stable solution
7	−1.9	$\frac{\partial p'}{\partial x} = 0$ in A	Oscillatory mode stabilize, unstable solution
8	−1.9	$\bar{w}\frac{\partial\theta'}{\partial z} = 0$ in A	Oscillatory mode stabilized, stable solution
9	0.5		Stable solution
10	−2	$K_v = 5\,\mathrm{m^2\,s^{-1}}$	Stable non-normal growth

4. Analysis of stable non-normal perturbation growth

Consider next the generalized stability of the front in the parameter regime where the eigenvalues of B are all smaller than 1 in absolute value, indicating that the specified background mean flow is stable to small perturbations. In this case, while all initial perturbations eventually decay, transient growth in the energy of initial perturbations can arise from the non-normality of the propagator (Farrell and Ioannou, 1996). As before, we take the background fields for this analysis from an average over the last 40 days of a 200 day integration of the nonlinear model at $t = 8$ h, but this time with the geostrophic velocity at the top of the domain set to $u_g = -2\,\mathrm{m\,s^{-1}}$ (experiment 2 in Table 1). The mean circulation for experiment 2 is quite similar to the circulation in experiment 1 (Figure 1). This specification leads to a stable propagator B (Eq. (10)). The energy growth factors for optimal perturbations in $\langle E_T\rangle$, $\langle E_p\rangle$ and $\langle E_k\rangle$ (Figures 2 and 3) reach their maximum as functions of the optimization time for $\tau = 0.4$ h. The energy growth of optimal perturbations in the stable case is significantly larger than that of the unstable mode in the first 2 h. We will see that in the stable case the growth mechanism of optimal initial perturbations is similar to the normal-mode instability mechanism discussed above, except during the first few minutes. The growth occurring over the first few minutes is made possible because the optimal is able to take

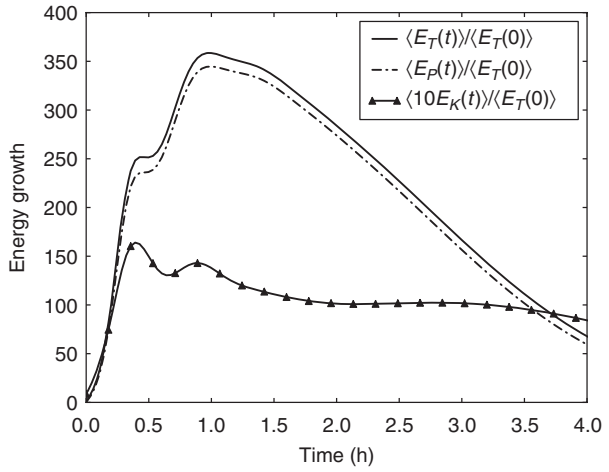

Figure 9. The growth of the normalized energy of the optimal initial perturbation for optimization time $\tau = 1$ h as a function of time. The growth factors for the total energy, potential energy and kinetic energy are shown; note that the kinetic energy growth factor is multiplied by 10.

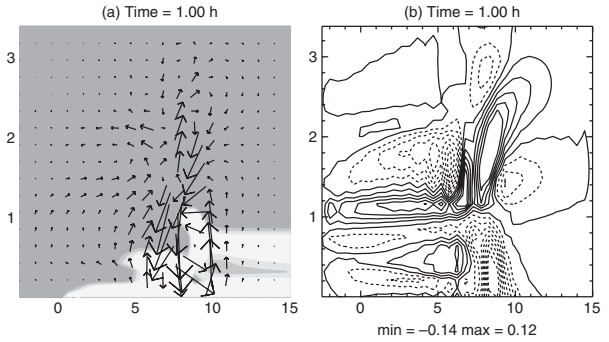

Figure 10. The optimal perturbation of experiment 2 at t = 1 h. Grey areas in (a) indicate $Ri > 0.25$, arrows denote u', w'. Contours in (b) are potential temperature. Solid contours are positive and dashed contours are negative.

advantage of physical mechanisms not available to the normal-mode instability. The energy growth (Figure 9) is impressively large, with the maximum total energy growth factor being 360. The maximum kinetic energy growth factor is 17 (note the factor of 10 applied to it in the figure), with the majority of the growth due to potential energy. The kinetic energy growth is of special interest because it is associated with the eddies shed behind the propagating front, which are seen in both observations and numerical experiments. Figure 10 shows the evolution at $t = 1$ h. The initial perturbation and its evolution in time are very similar to those of experiment 1 (Figures 4 and 5), indicating a similar growth mechanism. The eddies shed behind the front are more prominent in this experiment compared with the similar eddies in experiment 1. These eddies resemble the seaward-propagating K–H billows behind fronts in observations (Lapworth, 2000; Plant and Keith, 2007).

The fact that the non-normal growth mechanism differs from the normal-mode instability mechanism during the initial interval is best seen via the tendency terms in the energy equation (Eq. (9)) and Figure 12, where these terms are normalized by $\langle E_{\mathrm{T}}(t)\rangle$ and this normalization is indicated by (*). During the initial 15 min. the dominant terms affecting the normalized potential energy $\langle E_{\mathrm{p}}\rangle^*$ (Eq. (A3)) are $-\langle\alpha\theta' u' \partial\bar{\theta}/\partial x\rangle^*$ (solid line) and $\langle\theta'^2 \bar{u}\partial\alpha/\partial x\rangle^*$ (line denoted by + symbols). The first term reflects the formation of perturbation buoyancy by the advection of mean horizontal stratification by perturbation velocity around the front (Figure 11(a)). The second term reflects the propagation of perturbation buoyancy from its initial location within the stable boundary layer over the ocean to the weakly unstable area near the front, where α is much larger, leading to a large potential energy growth as shown in Figure 5(a) in the unstable case. Neither of these processes is available to modal K–H instability, which relies solely on vertical shear for its growth. The mechanism due to the second term is not exploited by the normal mode, which grows almost entirely away from the stable boundary layer over the ocean. After the first 15 min, the first-term mechanism continues to be important, while the second-term mechanism contribution to growth rapidly decreases.

Kinetic energy growth (Eq. (A2)) during the first 10 min (Figures 9 and 12(b)) is dominated by $-\langle u'u'\partial\bar{u}/\partial x\rangle^*$ and $-\langle u'w'\partial\bar{u}/\partial z\rangle^*$. The first term represents energy extraction associated with the mean strain rate in x, $\partial\bar{u}/\partial x$, which is not available to the classical normal mode K–H instability in purely vertical shear. The second term reflects the familiar extraction of kinetic energy from the mean vertical shear.

Beyond the first 15 min or so, the stable non-normal growth mechanism approaches the normal-mode instability mechanism discussed in the previous section. The spatial structure of these terms is shown in Figure 11(b) and (c) at $t = 1$ h. The term $-\langle u'u'\partial\bar{u}/\partial x\rangle^*$ is significant within box B (Figure 7) at the edge of the front where the horizontal gradient of $\bar{u}$ is largest. The extraction of kinetic energy by the term $-\langle u'w'\partial\bar{u}/\partial z\rangle^*$ is significant in box B, where the sea breeze has strong vertical shear, and in box A, where the return current has strong vertical shear.

In order better to understand normal versus non-normal growth, we use several diagnostics. One is to plot the normalized total energy rate of change $(\mathrm{d}E/\mathrm{d}t)/E$ as a function of time. For exponential growth or decay (normal modes) this quantity is a constant in time, yet it is non-constant for non-normal growth. Another diagnostic compares the rate of growth of a model variable with the known rate of growth of the fastest growing (or slowest decaying in the stable case) normal mode. Using these diagnostics, we find that the dynamics of optimal initial conditions are non-normal for the first 1.5 h in both stable and unstable regimes, while subsequently the dynamics approach the normal mode rate of growth or decay.

Non-normal perturbation growth exploits a greater variety of mechanisms than normal-mode growth. This is consistent with the above results in our model. In the case of normal-mode growth, the initial conditions must be such that they grow/decay exponentially in time. In the case of non-normal growth, the initial conditions may start out growing using one mechanism (e.g. the first 15 min of growth in Figure 12) and then switch to a different one, possibly similar to the normal growth mechanism, exactly as happens in our analysis. Thanks to this freedom to start with a different mechanism, the total non-normal growth may be much larger than the normal growth for initial perturbations of the same overall magnitude.

In the classical picture, $Ri < 0.25$ is a necessary condition for instability. Interestingly, the instabilities in our model are partially or completely contained in an area in which $Ri > 0.25$ (e.g. note the significant perturbation wind arrows in the shaded areas of Figure 6(b)). Similarly, in our stable case, the domain contains a region in which $Ri < 0.25$. This is an example of the known result that stability cannot be deduced from Ri alone (Farrell and Ioannou, 1993).

The alternating direction of eddies and pressure gradient within the boundary layer behind the front represents an oscillation with a period of about 2 h. This is qualitatively consistent with the observations of Donn *et al.* (1956), who found large-amplitude oscillations with periods of 25–40 min in the surface pressure after the passage of the sea-breeze front, although the period is longer in our simulations. The eddies span the moist boundary layer and the drier air above it and therefore mix the two air masses, as was observed by Xue *et al.* (1997), Lapworth (2000) and others.

4.1. *The role of the geostrophic wind in the instability process*

It is clear from previous studies that the synoptic-scale geostrophic wind over the region of the sea-breeze front influences the stability of sea-breeze fronts and the development of K–H eddies, but the

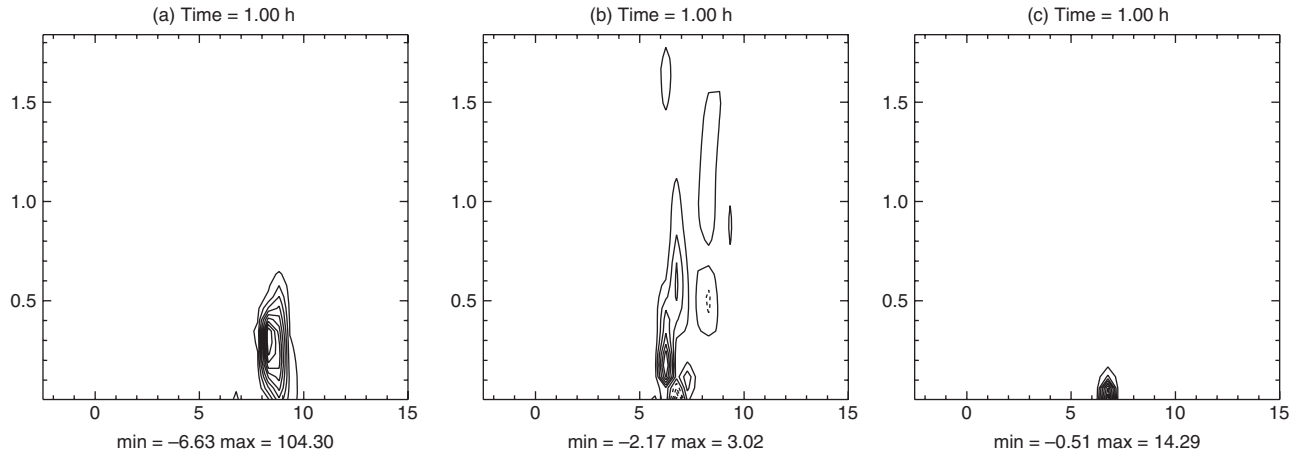

Figure 11. Contours of the dominant tendency terms in the energy equation (Eq. (9)). (a) $-\langle \alpha\theta' u' \frac{\partial \bar{\theta}}{\partial x} \rangle^*$. (b) $-\langle u' w' \frac{\partial \bar{u}}{\partial z} \rangle^*$. (c) $-\langle u' u' \frac{\partial \bar{u}}{\partial x} \rangle^*$.

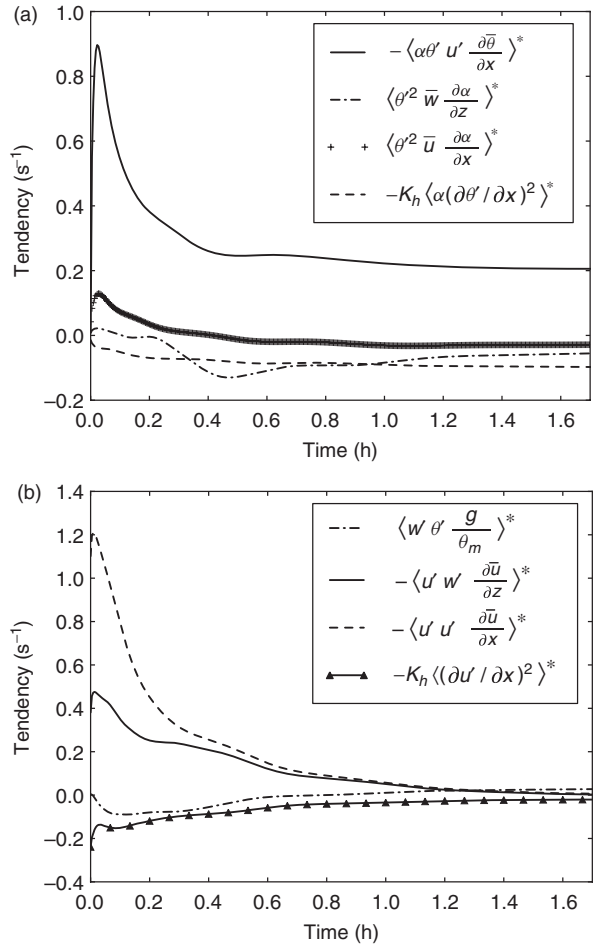

Figure 12. (a) Potential energy tendency terms multiplied by 100 in Eqs (8) and (9) for experiment 2. (b) The kinetic energy tendency terms multiplied by 1000 in the energy equation (Eqs (8) and (9)) for experiment 2. Additional terms in the energy equation (Eq. (9)) that are not plotted here are smaller by at least one order of magnitude than the ones shown.

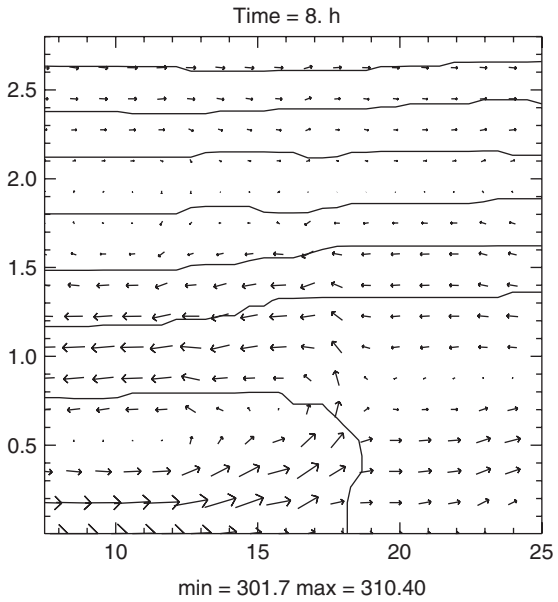

Figure 13. The sea-breeze circulation, with the geostrophic wind at the top of the domain set to $u_g = 50$, at the time during the day at which the front is most prominent. Note that the computational domain extends from −50 to 50 km and only part of it is plotted here, to allow us to concentrate on the front structure. Compare this with Figure 1(c) to see the effect of the geostrophic velocity on the front structure.

mechanism is still not understood (Plant and Keith, 2007). In this section we study front stability as a function of the geostrophic wind, keeping other parameter values as in experiment 1 above. We perform several calculations (experiments 1a–f, Table 1) with u_g varying between -3.5 and $1\,\mathrm{m\,s^{-1}}$. In these experiments we take the background fields to be an average over the last 10 days of a 30 day integration of the nonlinear model at $t = 8$ h. The propagator allows for significant non-normal growth and may be either stable or unstable in the normal-mode sense for $u_g \leq -1$, but shows no non-normal growth and is consistently stable for $u_g \geq -1\,\mathrm{m\,s^{-1}}$. Incidentally, the most unstable case is obtained for $u_g = -2.9\,\mathrm{m\,s^{-1}}$. The eigenvalue with the largest absolute value of the propagator B (Eq. (10)) is

$$\lambda = |\lambda| e^{i\phi} = \lambda_r + i\lambda_i = 1.000126 + 0.000173\,i.$$

This complex eigenvalue implies an oscillatory behaviour and translates into an exponential growth time of about 2.2 h and an oscillation period of 10.1 h. The stable case with the largest energy growth is obtained for $u_g = -2.85\,\mathrm{m\,s^{-1}}$, very close to u_g of the most unstable case. The maximum total energy growth factor in this case is 620 and the maximum factor of kinetic energy growth is 43. The oscillation period is 2 h.

There are two main points to notice in this context. First, changing the geostrophic wind leads to substantial changes in the front structure (compare Figures 1(c) and 13). This, in turn, changes the propagation of perturbations, which influences the establishment of the absolute instability, resulting in transition from stable to unstable regimes.

The stability behaviour as a function of u_g can be explained as follows. When $u_g \geq -1\,\mathrm{m\,s^{-1}}$, and especially when it is positive, the mean flow (Figure 13) advecting the anomalies is modified. Specifically, the growing θ' anomalies that develop at the sea-breeze front within the boundary layer (region B in Figure 7) are advected in this case inland instead of upward into region A as

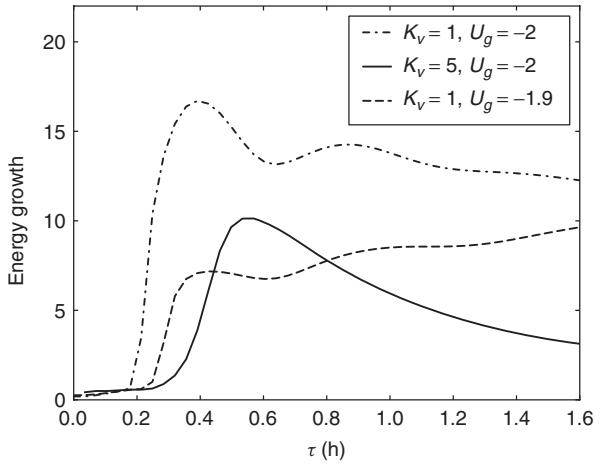

Figure 14. Kinetic energy growth factor as a function of optimization time τ. The results of experiment 2, where the propagator is stable, experiment 1, where the propagator is unstable, and experiment 10, where $K_v = 5\,m^2\,s^{-1}$, are shown.

they are in experiment 1 (Figure 1). Similarly, the u' anomalies are advected inland and do not lead to a large w' in region A. The anomalies in A are therefore not amplified and this breaks the feedback loop described in section 3 and stabilizes the flow (experiment 5, Table 1).

These experiments demonstrate that the transition from an infinite domain to a finite one makes the normal-mode K–H instability vulnerable. In a finite domain, the feedback loop between regions A and B is critical to the existence of instability and small parameter changes that affect this loop can lead to the stabilization of the flow.

4.2. *Sensitivity to the vertical eddy coefficient*

In our analysis above, the vertical eddy coefficient (for both heat and momentum) was $K_v = 1\,m^2\,s^{-1}$, while in some cases one might expect it to be significantly larger in a turbulent front scenario. In order to examine the sensitivity to this value, we performed experiment 10, using the same parameters as in our standard stable experiment 2 except for an increase of K_v by a factor of 5 to $K_v = 5\,m^2\,s^{-1}$. The general evolution looks very similar to that of experiment 2 but, with the strong damping due to the larger dissipation, the maximum of the total energy growth factor is reduced by a factor of 5 and that of the kinetic energy by a factor of 2 (Figure 14). The same figure also shows the kinetic energy growth obtained in our standard unstable experiment 1 where $u_g = -1.9\,m\,s^{-1}$; the maximum growth of the kinetic energy in the first hour is smaller in this standard unstable experiment than in both cases with $u_g = -2\,m\,s^{-1}$, where $K_v = 1$ and $5\,m^2\,s^{-1}$. This indicates that our result showing that the non-normal stable growth can be larger than the unstable growth is not sensitive to the vertical eddy coefficient.

5. Conclusions

We examined the generalized stability of a sea-breeze front in both stable and unstable regimes. Our objectives were to understand the mechanism of normal-mode instability, which exists in part of the parameter regime, and the mechanism of transient non-normal growth, which is found for many other model parameter values, and also to study the role of the geostrophic wind above the front region.

By calculating stability explicitly using the eigenvalues of the linearized model dynamics, we showed that areas of $Ri < 0.25$ do not imply that the dynamics are necessarily unstable. We further showed that even when the model is stable there exists a large amplification of initial conditions, via the mechanism of non-normal transient growth (Farrell and Ioannou, 1993, 1996). This amplification leads to the shedding of eddies behind the sea-breeze front, as seen in observations, laboratory experiments and numerical models of the sea breeze and other gravity-current fronts.

The amplification mechanism relies on a feedback loop that is required for normal-mode instability because of the finite extent of the sea-breeze domain. This amplification mechanism is more readily analyzed in the unstable regime, where we explore it in detail. The regime may be shifted from stable to unstable by adjusting a geostrophic wind specified at the top of our domain. The instability may be understood by dividing the sea-breeze front area into the two rectangular areas marked in Figure 7, covering its lower part (including the sea breeze within boundary layer) and upper part (the return current). Anomalies in the upper part grow by advection of the mean flow momentum and stratification by the vertical flow of the perturbation. However, because anomalies propagate away from the finite area with vertical shear in this case, they would decay in the absence of some additional feedback.

This additional feedback required for modal instability is found to act through the lower part of the sea-breeze front. Temperature anomalies in the upper part induce pressure gradients in the lower part. These lead to growth of both the horizontal wind and the vertical wind. The vertical wind component then enters the upper area and re-excites the growth there, closing the feedback loop and leading to both normal-mode instability and non-normal growth in the stable regime.

We find that this instability mechanism is robust, yet vulnerable to some parameter changes that weaken this feedback loop. We emphasize that stability cannot be deduced merely using the Richardson number criterion and that strong transient growth of perturbations may be achieved even in the absence of normal-mode instability. Our standard experiment is based on an assumed constant-stress surface layer, following standard assumptions and observations. We also examined the evolution with an alternative no-slip boundary condition at the lower boundary. Finally, we considered sensitivity to the vertical eddy coefficient in range $K_v = 1$–$5\,m^2\,s^{-1}$. The results again show robustness of our findings to all of these model changes.

When the model is put in a parameter regime that is stable to small perturbations, it may still display very dramatic transient amplification of both potential and kinetic energy of initial perturbations via non-normal growth. Specifically, the non-normal growth and propagation of eddies that we find to occur above the boundary layer, when the model is stable and in regions with $Ri > 0.25$ (e.g. Figure 4), is consistent with observations (Lapworth, 2000) and numerical simulations (Sha *et al.*, 1991; Xue *et al.*, 1997). A ratio of 4.4–7.5 between the horizontal wavelength of the growing perturbation and the thickness h of the shear layer is often used as evidence of K–H instability when $Ri < 0.25$ (Droegemeier and Wilhelmson, 1987; Mueller and Carbone, 1987; Sha *et al.*, 1991). In our analysis, the height range of the return flow is about 0.5 km, part of this flow is found in the region where $Ri < 0.25$ and the diameter of the developing eddies is 2–3 km, as in figure 7 of Sha *et al.* (1991), implying a wavelength about eight times the depth of the shear layer. Yet our flow is stable, as verified by the eigenvalues of the propagator, indicating that this criterion for deducing the existence of K–H instability may not be universally valid and should be used with care.

Based on our analysis, we suggest that K–H instability may not necessarily be occurring in observations, numerical models and laboratory experiments of sea breezes and other spatially confined gravity currents that show the amplification of initial anomalies. The classical K–H mode instability assumes the unstable domain to be infinite in extent, so that the distinction between absolute and convective instability does not arise (Briggs, 1964; Merkine, 1977; Farrell, 1982). However, this is not the case for the sea-breeze front. For instability in such a limited domain, an absolute instability is required; this requires additional feedbacks, as we find here, implying a normal-mode growth mechanism that may be substantially different from that of the classical K–H

normal-mode instability. Transient growth in a stable parameter regime, on the other hand, quite generally leads to a dramatic amplification of initial perturbations.

This study is based on the assumption of along-coast symmetry. Observed fronts are, of course, never completely symmetric, and it would be interesting and important to extend this work to study the effects of along-axis asymmetry. It would also be interesting to examine the role of some additional parameters such as the amplitude of the ground surface temperature θ_0, the turbulent Prandtl number (ratio between momentum eddy diffusivity and heat-transfer eddy diffusivity), turbulent eddy diffusivity and heat-transfer eddy diffusivity, which depend on stratification.

Acknowledgements

ET and YF were supported by the NSF climate dynamics program, grant ATM-0754332. BF was supported by NSF ATM-0736022. ET thanks the Weizmann Institute for its hospitality during parts of this work.

Appendix: The numerical model

The numerical algorithm of the model used here is described in Feliks (2004) and Feliks *et al.* (2010). Horizontal advection terms are approximated in the nonlinear model by the four-point upwind scheme and in the linear model by centre differencing. The equations are applied to a staggered grid contained within a vertical plane extending in the x coordinate perpendicular to the sea-surface temperature front. The horizontal grid interval was taken as dx = 0.5 km and 200 grid points were utilized, covering a domain size of 100 km. 38 vertical levels are used at heights of 0, 2.5, 5, 10, 20, 40, 80, 160, 240, 320, 400, 480, 560, 640, 720, 800, 880, 960, 1040, 1120, 1200, 1360, 1680, 1840, 2000, 2160, 2320, 2480, 2640, 2880, 2960, 3120, 3380, 3520, 3840, 4160, 4480, 4800 and 5120 m. The time step for the nonlinear model is $\Delta t = 20$ s.

The value of the vertical diffusivity K_v used in the model is appropriate to neutral and stable conditions. In unstable cases, found mainly ahead of the sea-breeze front during the daytime, the values of K_v can be larger by two orders of magnitudes. Therefore, vertical diffusion with the values we are using for K_v cannot adjust the atmospheric column in real time and we parametrize the adjustment to account for this. The convective adjustment is done as follows: in each column we find the height z_i where, below z_i, the potential temperature is, after adjustment, determined by

$$\theta(z_i) = \theta(z=0) + 10^{-2} z \tag{A1}$$

(where z is given in km) and, above z_i, $\partial\theta/\partial z \geq 10^{-2}$. To find the height z_i we begin in the lowest level: we first check if $\partial\theta/\partial z < 10^{-2}$, then we substitute θ at this level according to Eq. (A1) and proceed to the next upper level with the same procedure; if $\partial\theta/\partial z \geq 10^{-2}$ then z_i is the height of the current level. The potential energy and the energy-norm kernel X are relevant only when the stratification is positive. Thus, when the atmosphere has neutral stratification, we used a very weak stable state. We checked the sensitivity of the solution to the value of the minimum stratification and found that decreasing the minimum stratification by an order of magnitude barely changed the results.

Our lower boundary condition given in the main text is a specified surface drag, corresponding to a constant-stress surface layer within the lowermost model grid box. Within this first grid box, K_v is therefore implicitly a function of z. Above the surface layer, K_v and K_h are constant in order to simplify the analysis. The main normal and non-normal growth mechanisms explored in this article should be well described by this approximation.

In this model, as in many numerical and analytical models of the sea breeze, the specified ground temperature includes only the first Fourier component in time (e.g. Estoque, 1961; Sha *et al.*, 1991; Feliks, 2004). Adding the second Fourier component leads to a more accurate timing of the land warming relative to sunrise time, yet does not change the evolution of the sea breeze significantly, since the amplitude of the second component is about 0.25 times that of the first component.

The model linearized about the steady secondary circulation is integrated in a partial domain with 35 grid points in the horizontal direction and 34 vertical levels, at the same heights as in the nonlinear model, between 0 and 3520 m. The time step in the linearized model is $\Delta t = 1$ s, while all other numerical and physical parameters were the same as in the fully nonlinear model. While the nonlinear model uses $\Delta t = 20$ s, the smaller time step of the linear model allows the accurate calculation of the eigenvalues of the propagator corresponding to all time-scales.

The domain-averaged kinetic energy equation is obtained by multiplying the u' equation (Eq. (5)) by u' and the v' equation by v', integrating the sum over the domain and dividing by the domain area. Utilizing the boundary conditions, we find

$$\begin{aligned}\frac{\partial\langle E_\mathrm{k}\rangle}{\partial t} =& \frac{1}{2}\frac{\partial}{\partial t}(\langle u'^2\rangle + \langle v'^2\rangle) = -\left\langle u'^2\frac{\partial\bar{u}}{\partial x}\right\rangle - \left\langle u'w'\frac{\partial\bar{u}}{\partial z}\right\rangle \\ &- \left\langle v'u'\frac{\partial\bar{v}}{\partial x}\right\rangle - \left\langle v'w'\frac{\partial\bar{v}}{\partial z}\right\rangle + \left\langle w'\theta'\frac{g}{\theta_\mathrm{m}}\right\rangle \\ &- K_\mathrm{h}\left(\left\langle\left(u'_x\right)^2\right\rangle + \left\langle\left(v'_x\right)^2\right\rangle\right) \\ &- K_\mathrm{v}\left(\left\langle\left(u'_z\right)^2\right\rangle + \left\langle\left(v'_z\right)^2\right\rangle\right) \\ &+ \left\{\left[\frac{1}{\rho_\mathrm{m}}u'p' + \bar{u}u'^2 + \bar{u}v'^2 + \bar{u}\alpha\theta'^2\right]\right\}_{x_w}^{x_\mathrm{e}}. \end{aligned} \tag{A2}$$

The domain-averaged available potential energy equation is obtained by multiplying the θ' equation (Eq. (5)) by $\alpha\theta'$ with

$$\alpha = g\left(\theta_\mathrm{m}\frac{\partial\bar{\theta}}{\partial z}\right)^{-1},$$

integrating over the domain and dividing by the domain area. Using the boundary conditions, we find

$$\begin{aligned}\frac{\partial\langle E_\mathrm{P}\rangle}{\partial t} =& \frac{1}{2}\frac{\partial}{\partial t}\langle\alpha\theta'^2\rangle = -\langle\alpha\theta'u'\frac{\partial\bar{\theta}}{\partial x}\rangle - \langle w'\theta'\frac{g}{\theta_\mathrm{m}}\rangle \\ &+ \frac{1}{2}\left\langle\left(\theta'^2\bar{u} + K_\mathrm{h}\frac{\partial\theta'^2}{\partial x}\right)\frac{\partial\alpha}{\partial x}\right\rangle \\ &+ \frac{1}{2}\left\langle\left(\theta'^2\bar{w} + K_\mathrm{v}\frac{\partial\theta'^2}{\partial z}\right)\frac{\partial\alpha}{\partial z}\right\rangle \\ &- K_\mathrm{h}\left\langle\alpha\left(\theta'_x\right)^2\right\rangle - K_\mathrm{v}\left\langle\alpha\left(\theta'_z\right)^2\right\rangle \\ &+ \left\{\left[\bar{u}\alpha\theta'^2\right]\right\}_{x_w}^{x_\mathrm{e}}. \end{aligned} \tag{A3}$$

References

Atkinson B. 1981. *Meso-Scale Atmospheric Circulations*. Academic Press: New York, NY.

Benjamin T. 1968. Gravity currents and related phenomena. *J. Fluid Mech.* **31**: 209–248.

Briggs RJ. 1964. *Electron-Stream Interaction with Plasmas*. Cambridge University Press: Cambridge, UK.

Britter R, Linden P. 1980. The motion of the front of a gravity current travelling down an incline. *J. Fluid Mech.* **99**: 531–543.

Britter R, Simpson J. 1978. Experiments on the dynamics of a gravity current head. *J. Fluid Mech.* **88**: 223–240.

Britter R, Simpson J. 1981. A note on the structure of the head of an intrusive gravity current. *J. Fluid Mech.* **112**: 459–466.

Buckley RL, Kurzeja RJ. 1997a. An observational and numerical study of the nocturnal sea breeze. part i: Structure and circulation. *J. Appl. Meteorol.* **36**: 1577–1598.

Buckley RL, Kurzeja RJ. 1997b. An observational and numerical study of the nocturnal sea breeze. part ii: Chemical transport. *J. Appl. Meteorol.* **36**: 1599–1619.

Donn W, Milic P, Brilliant R. 1956. Gravity waves and the tropical sea breeze. *J. Meteorol.* **13**: 356–361.

Drazin P. 1958. The stability of a shear layer in an unbounded heterogeneous inviscid fluid. *J. Fluid Mech.* **4**: 214–224.

Droegemeier K, Wilhelmson R. 1987. Numerical-simulation of thunderstorm outflow dynamics. 1. Outflow sensitivity experiments and turbulence dynamics. *J. Atmos. Sci.* **44**: 1180–1210.

Estoque M. 1961. A theoretical investigation of the sea breeze. *Q. J. R. Meteorol. Soc.* **87**: 136–146.

Farrell BF. 1982. Pulse asymptotics of the Charney baroclinic instability problem. *J. Atmos. Sci.* **39**: 507–517.

Farrell B. 1988. Optimal excitation of neutral Rossby waves. *J. Atmos. Sci.* **45**: 163–172.

Farrell B. 1989. Optimal excitation of baroclinic waves. *J. Atmos. Sci.* **46**: 1193–1206.

Farrell B, Ioannou P. 1993. Transient development of perturbations in stratified shear-flow. *J. Atmos. Sci.* **50**: 2201–2214.

Farrell BF, Ioannou PJ. 1996. Generalized stability theory part I: Autonomous operators. *J. Atmos. Sci.* **53**: 2025–2040.

Feliks Y. 1988. The sea-breeze front analytical model. *J. Atmos. Sci.* **45**: 1030–1038.

Feliks Y. 2000. An analytical model of gravity currents in a stable atmosphere. *J. Fluid Mech.* **420**: 27–46.

Feliks Y. 2004. Nonlinear dynamics and chaos in the sea and land breeze. *J. Atmos. Sci.* **61**: 2169–2187.

Feliks Y, Tziperman E, Farrell B. 2010. Nonnormal frontal dynamics. *J. Atmos. Sci.* **67**: 1218–1231, doi: 10.1175/2009JAS3214.1.

Jeričević A, Večenaj Ž. 2009. Improvement of vertical diffusion analytic schemes under stable atmospheric conditions. *Boundary Layer Meteorol.* **131**: 293–307.

Lapworth A. 2000. Observations of atmospheric density currents using a tethered balloon-borne turbulence probe system. *Q. J. R. Meteorol. Soc.* **126**: (A): 2811–2850.

Linden P, Simpson J. 1986. Gravity-driven flows in a turbulent fluid. *J. Fluid Mech.* **172**: 481–497.

Maxworthy T, Leilich J, Simpson J, Meiburg E. 2002. The propagation of a gravity current into a linearly stratified fluid. *J. Fluid Mech.* **453**: 371–394, doi: 10.1017/S0022112001007054.

Merkine LO. 1977. Convective and absolute instability of baroclinic eddies. *Geophys. Astrophys. Fluid Dyn.* **9**: 129–157, doi: 10.1080/03091927708242322.

Miles J, Howard L. 1964. Note on a heterogeneous shear flow. *J. Fluid Mech.* **20**: 331–336.

Mueller C, Carbone R. 1987. Dynamics of a thunderstorm outflow. *J. Atmos. Sci.* **44**: 1879–1898.

Neumann J, Mahrer Y. 1971. Theoretical study of land and sea breeze circulation. *J. Atmos. Sci.* **28**: 532–542.

Pearson R. 1973. Properties of sea breeze front as shown by a numerical model. *J. Atmos. Sci.* **30**: 1050–1060.

Physick W. 1976. Numerical-model of sea-breeze phenomenon over a lake or gulf. *J. Atmos. Sci.* **33**: 2107–2135.

Plant RS, Keith GJ. 2007. Occurrence of Kelvin–Helmholtz billows in sea-breeze circulations. *Boundary Layer Meteorol.* **122**: 1–15, doi: 10.1007/s10546-006-9089-x.

Rao P, Fuelberg H. 2000. An investigation of convection behind the cape canaveral sea-breeze front. *Mon. Weath. Rev.* **128**: 3437–3458.

Sha W, Kawamura T, Ueda H. 1991. A numerical study on sea land breezes as a gravity current –Kelvin–Helmholtz billows and inland penetration of the sea-breeze front. *J. Atmos. Sci.* **48**: 1649–1665.

Simpson J. 1969. A comparison between laboratory and atmospheric density currents. *Q. J. R. Meteorol. Soc.* **95**: 758–765.

Simpson J. 1972. Effects of the lower boundary on the head of a gravity current. *J. Fluid Mech.* **53**: 759–768.

Simpson J, Linden P. 1989. Frontogenesis in a fluid with horizontal density gradients. *J. Fluid Mech.* **202**: 1–16.

Xu Q, Xue M, Droegemeier K. 1996. Numerical simulations of density currents in sheared environments within a vertically confined channel. *J. Atmos. Sci.* **53**: 770–786.

Xue M, Xu Q, Droegemeier K. 1997. A theoretical and numerical study of density currents in nonconstant shear flows. *J. Atmos. Sci.* **54**: 1998–2019.

